Linear Magnetoresistance Caused by Mobility Fluctuations in *n*-Doped Cd_3As_2

A. Narayanan,[1] M. D. Watson,[1] S. F. Blake,[1] N. Bruyant,[2] L. Drigo,[2] Y. L. Chen,[1] D. Prabhakaran,[1] B. Yan,[3] C. Felser,[2] T. Kong,[4,5] P. C. Canfield,[4,5] and A. I. Coldea[1,*]

[1]*Department of Physics, Clarendon Laboratory, University of Oxford, Parks Road, Oxford OX1 3PU, United Kingdom*
[2]*Laboratoire National des Champs Magnetiques Intenses (CNRS), 31077 Toulouse, France*
[3]*Max-Planck-Institut fur Chemische Physik fester Stoffe, 01187 Dresden, Germany*
[4]*Ames Laboratory, Iowa State University, Ames, Iowa 50011, USA*
[5]*Department of Physics and Astronomy, Iowa State University, Ames, Iowa 50011, USA*

(Received 12 December 2014; published 19 March 2015)

Cd_3As_2 is a candidate three-dimensional Dirac semimetal which has exceedingly high mobility and nonsaturating linear magnetoresistance that may be relevant for future practical applications. We report magnetotransport and tunnel diode oscillation measurements on Cd_3As_2, in magnetic fields up to 65 T and temperatures between 1.5 and 300 K. We find that the nonsaturating linear magnetoresistance persists up to 65 T and it is likely caused by disorder effects, as it scales with the high mobility rather than directly linked to Fermi surface changes even when approaching the quantum limit. From the observed quantum oscillations, we determine the bulk three-dimensional Fermi surface having signatures of Dirac behavior with a nontrivial Berry phase shift, very light effective quasiparticle masses, and clear deviations from the band-structure predictions. In very high fields we also detect signatures of large Zeeman spin splitting ($g \sim 16$).

DOI: 10.1103/PhysRevLett.114.117201 PACS numbers: 75.47.-m, 71.18.+y, 74.25.Jb

A three-dimensional (3D) Dirac semimetal is a three-dimensional analogue of graphene, where the valence and conduction bands touch at discrete points in reciprocal space with a linear dispersion. These special points are protected from gap formation by crystal symmetry, and such a topologically nontrivial band structure may harbor unusual electronic states. A Dirac semimetal may be tuned to attain a Weyl semimetal phase through breaking of inversion or time reversal symmetry [1]. Alternatively, if the symmetry protection from gapping is removed, a three-dimensional topological insulator could be stabilized on the surface [1]. Three-dimensional Dirac semimetals are rare, and an opportunity to realize such a state in Cd_3As_2 has generated a lot of interest. Surface probes, such as ARPES and STM [2–5], found that the linear dispersion extends up to high energy 200–500 meV, strongly dependent on the cleavage directions [6]. Furthermore, the large nonsaturating linear magnetoresistance (MR) found in Cd_3As_2 [7,8] in high-mobility samples was assigned to the lifting of protection against backscattering caused by possible field-induced Fermi surface changes [7,8].

In this Letter, we report a magnetotransport study in high magnetic fields up to 65 T of *n*-doped Cd_3As_2 approaching the quantum limit that reveal no discernible Fermi surface change except those caused by the large Zeeman splitting. We observe Shubnikov–de Haas (SdH) quantum oscillations that allow us to characterize the three-dimensional Fermi surface and its relevant parameters. The observed linear MR in ultrahigh magnetic fields and the values of the linear magnetoresistance are closely linked to the mobility field scale. This suggests that the unconventional, nonsaturating, large, and linear magnetoresistance in our electron-doped crystals of Cd_3As_2 is likely to originate from mobility fluctuations caused by As vacancies. We also discuss the deviations of experiments from the standard density functional theory calculations.

Methods.—Crystals of Cd_3As_2 were grown by both solid state reaction and solution growth from a Cd-rich melt due to its very narrow growth window [9,10]. X-ray diffraction shows that our single crystals of Cd_3As_2 crystallize in the tetragonal symmetry group $I4_1/acd$ with lattice parameters $a = 12.6595(6)$ Å and $c = 25.4557(10)$ Å, cleaving preferentially in the (112) plane, in agreement with previous studies [9] (see Supplemental Material [11]). Band-structure calculations were performed with WIEN2K including the spin-orbit coupling [12] using the structural details from Ref. [9]. We have performed magnetotransport measurements in the standard Hall and resistivity configuration using the ac lock-in technique by changing the direction of the magnetic field **B** to extract the symmetric (ρ_{xx}) and the antisymmetric (ρ_{xy}) component of the resistivity tensor, respectively. The transverse magnetoresistance ($I \perp B$) was measured for different orientations, θ being the angle between **B** and the normal to the (122) plane. Measurements were conducted on three different batches (a, b, and c), mostly on crystals from batch a (S_1^a, S_2^a, etc.) having the lowest carrier concentration. Measurements were performed at low temperatures (1.5 K) in steady fields up to 18 T in Oxford and in pulsed fields up to 65 T at the LNCMI, Toulouse. We also measured skin depth in pulsed fields using a tunnel diode oscillator technique (TDO) by recording the change in frequency of an LC tank circuit with the sample wound in a copper coil, reported data being corrected for the magnetoresponse of the empty coil.

Figure 1(a) shows the magnetoresistance $\Delta\rho_{xx}(B)/\rho_{xx}(0)$ as a function of the magnetic field up to 65 T for sample S_2^a at fixed temperatures between 4 and 300 K. The MR is linear and unusually large, ~2000%, and shows a strong temperature dependence. Both the resistance and the magnetoresistance change by a factor of 5 from 300 to 4 K [inset in Fig. 1(a)], and the link between these two quantities will be discussed in detail later. Figure 1(b) shows the Hall component ρ_{xy} up to 18 T for S_1^a up to 75 K (raw data also in Ref. [11]). Quantum oscillations are discernible, on a highly linear background, from as low as 3 T with a characteristic frequency varying for different samples between 30 and 50 T, shown in Figs. 1(c)–1(e) and listed in Table I. Spin-splitting effects are evident in very high magnetic fields approaching the quantum limit ($n = 1$) in Fig. 1(c). The field dependence of the resonant frequency from TDO measurements for sample S_2^c is shown in Fig. 1(d) together with subtracted quantum oscillations. This frequency variation ΔF_{TDO} tracks the change in impedance of the coil and is a measure of the skin depth of the sample, $\delta \propto \rho_{xx}^{0.5}$.

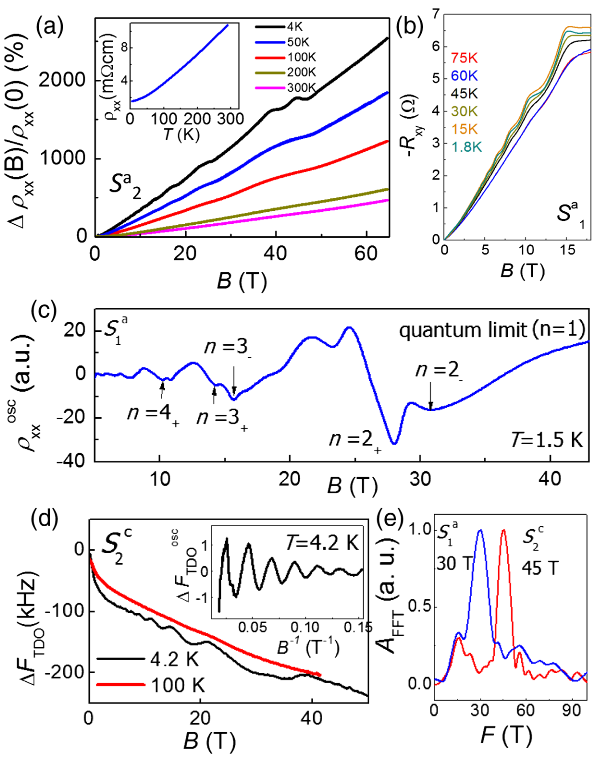

FIG. 1 (color online). High magnetic field data. (a) Field dependence of ρ_{xx} and the relative change in magnetoresistance, $\Delta\rho_{xx}/\rho_{xx}(0)$, for sample S_2^a up to 65 T for temperatures between 4 and 300 K. (b) Field dependence of Hall resistance, R_{xy}, for sample S_1^a up to 18 T. (c) The oscillatory part of symmetrized ρ_{xx} for S_2^a approaching the quantum limit. The arrows indicate the positions of different spin-split Landau levels crossing the Fermi level. (d) The field dependence of the resonant frequency, ΔF_{TDO}, of a tunnel diode oscillator for sample S_2^c up to 55 T. The inset shows the oscillatory part of ΔF_{TDO}. (e) FFT frequencies corresponding to the oscillatory signal at low temperatures from (c) for S_2^a and the inset in (d) for S_2^c.

Quantum oscillations.—The quantum oscillations in conductivity are given by $\Delta\sigma_{xx} \propto \cos\{2\pi[(F/B) - \frac{1}{2} + \beta]\}$, where β is the Berry phase and F is the SdH frequency of the oscillations, corresponding to an extremal area of the Fermi surface perpendicular to the magnetic field B. Figure 2(a) shows the angular dependence of SdH frequencies by rotating away from the (112) plane for different samples. The SdH frequencies show very little variation as a function of the orientation in the magnetic field, from 31 to 45 T for sample S_1^a (see also Table I). This behavior is expected for a three-dimensional elliptical Fermi surface with a k_F vector, extracted from the Osanger relationship $F = \hbar\pi k_F^2/(2\pi e)$ and varying between $k_F = 0.03$ and 0.04 Å^{-1}. These values give a very small carrier concentration of $n_{\mathrm{SdH}} = 1.0(2) \times 10^{18}$ cm^{-3}, consistent with that from Hall measurements $n_{\mathrm{Hall}} = 1.8 \times 10^{18}$ cm^{-3} [extracted from R_{xy} in Fig. 1(b) as discussed in Ref. [13]], assuming two elliptical pockets, as shown in Table I. A Lifshitz transition as a function of doping occurs from two small elliptical Fermi surfaces centered at the Dirac node ($k_z \sim 0.15$ Å^{-1} away from Γ) [4] to a larger merged elliptical Fermi surface centered now at Γ (see [11]). Band-structure calculations suggest that this transition should occur very close to the Fermi level (~10 meV), whereas in the surface experiments it is not seen up to 300 meV [4,5] [see the inset in Fig. 2(c) and Ref. [11]). This discrepancy between the band structure and experiments is rather surprising and requires further understanding.

The temperature dependence of the amplitude of the quantum oscillations up to 90 K can be used to extract the values of the effective cyclotron mass m_{eff}, using the standard Lifshitz-Kosevich formalism [14], with the thermal damping term $R_T = T/\sinh(X)$ with $X = 2\pi^2 T m_{\mathrm{eff}}/\hbar e B$, which also holds for the Dirac spectrum [15,16], as shown in Fig. 2(b). For parabolic bands, one would expect m_{eff} to be constant as a function of doping, while for Dirac bands $m_{\mathrm{eff}} = \hbar k_F/v_F$. The measured effective mass extracted for our samples from different batches varies from 0.023 to 0.043m_e, increasing with F and the corresponding carrier concentration n_{SdH}, as listed in Table I. This suggests a deviation from a parabolic band dispersion, whereas the high-mobility values found in Cd_3As_2 point usually towards a linear dispersion. Having samples with different concentrations, one could attempt to extract the Fermi velocity v_F directly from the slope of $1/m_{\mathrm{eff}}$ versus k_F^{-1}, shown in Fig. 2(c), which gives a finite intercept suggesting a departure from a perfect Dirac behavior [possibly linked to band-structure effects that show holelike

TABLE I. Band parameters extracted from quantum oscillations, such as frequencies for two different orientations (F_1 for $B \parallel [112]$ axis and F_2 for $B \perp [112]$), Fermi velocities, $v_F = \hbar k_F / m_{\rm eff}$, the Berry phase β, the g factor, the Dingle temperature T_D, the mean free path ℓ, and the quantum mobility μ_q. The carrier concentration $n_{\rm SdH}$ was estimated by assuming that the Fermi surface is a three-dimensional ellipsoid. The Hall effect data give the carrier concentration $n_{\rm Hall}$ and classical mobilities μ_c and the mobility ratio μ_c/μ_q. The data are reported for samples from different batches (a, b, and c), and they are compared to published data.

	F_1 T	F_2 T	$n_{\rm SdH}$ 10^{18} cm^{-3}	$n_{\rm Hall}$ 10^{18} cm^{-3}	$m_{\rm eff}$ m_e	v_F 10^6 m/s	T_D K	ℓ nm	μ_q m^2/V s	μ_c m^2/V s	μ_c/μ_q	g	β π
S_1^a	31(4)	45(4)	1.0(2)	1.8(2)	0.023(4)	1.54(4)	15.4(8)	122(8)	0.60(1)	8.0(5)	13.3(4)	16(4)	0.83(8)
S_1^b	42(4)	52(4)	1.5(2)	2.5(2)	0.031(3)	1.33(4)	14.4(8)	112(8)	0.47(1)	3.4(3)	7.1(4)	15(3)	1.08(6)
S_1^c	67(4)	74(4)	3.1(2)	3.8(2)	0.043(4)	1.21(4)	9.8(8)	150(8)	0.51(1)	2.9(3)	5.7(4)	⋯	0.84(4)
Lit.	20–90	20–90	0.1–8	2–20	0.03–0.08	0.4–12	11–17	⋯	0.1–10^4	1–10^3	1–10^4	2–100	⋯
Refs.	[7,23]	[23]	[7,8]	[7,8]	[7,23]	[2,23]	[24]	⋯	[7,8]	[8]	[8]	[5,17,18]	⋯

bending towards Γ (see [11])]. The estimation of $v_F \approx 4 \times 10^6$ is similar to those extracted from ARPES, $vf \sim 0.8$–1.5×10^6 m/s [2,4], with deviations caused by orbitally averaged effects (see also Table I). We have also extracted the values of the g factor from the spin-split oscillations visible at high fields [see Fig. 1(c)], corresponding to the spin-up and spin-down Landau levels ($\pm g\mu_B B$) that cross the Fermi level and give a large value of $g \sim 16(4)$, consistent with previous reports [17,18].

The Berry phase β can take values of $\beta = 0$ for parabolic dispersion and $\beta = \pi$ for a Dirac point [19]. To extract the Berry phase, we use the conductivity σ_{xx} by measuring both ρ_{xx} and ρ_{xy} simultaneously (see [11]) and inverting the resistivity tensor, as shown in the inset in Fig. 2(d). The direct fit of $\Delta\sigma_{xx}$ gives a value of $\beta = 0.84(8)\pi$ for S_2^a, in agreement with previous reports [20], as shown in Table I. Another method to extract β is given by the linear intercept of an index plot of the conductivity minima versus the inverse magnetic field; for samples S_1^a and S_2^a in the low-field region (from $n = 4$), that gives $\beta = 0.8(1)\pi$ [solid line in Fig. 2(d)]. In high magnetic fields, the positions of the minima are strongly affected by the spin splitting, and a nonlinear fan diagram analysis detailed in Refs. [19,21] gives $\beta = 0.9(1)\pi$ for S_2^a [dashed line in Fig. 2(d)].

Scattering.—The field dependence of the amplitude of quantum oscillations at fixed temperatures [inset in Fig. 2(b)] gives access to the Dingle temperature, which is a measure of the field-dependent damping of the quantum oscillations due to impurity scattering. For sample S_1^a the quantum scattering time given by $\tau_q = \hbar/(2\pi k_B T_D)$ corresponds to a quantum mobility of $\mu_q \sim 6000$ cm^2/V s and a mean free path $\ell_q = v_F \tau_q$ of $\sim 122(8)$ nm. These values are in good agreement with some of the reports for single crystals and thin films, as shown in Table I. Another way to estimate the mobility is to apply a simple Drude model to the Hall and resistivity data. By using the carrier concentration estimated from the Hall effect $n_H = 1.8 \times 10^{18}$ cm^{-3} and $\rho_{xx0} = 42$ $\mu\Omega$ cm for sample S_1^a (shown in Ref. [11]), the classical mobility from $1/\rho_{xx} = n_H \mu_c e$ is $\mu_c = 80000$ cm^2/V s, a factor up to 13 larger than the mobility from quantum oscillations, μ_q. This difference in the two mobilities is common, as they measure different scattering processes. The SdH estimated mobility is affected by all processes that cause the Landau level broadening—i.e., quantum scattering time τ_q measures how long a carrier stays in a momentum eigenstate—whereas the classical Drude mobility is affected only by scattering

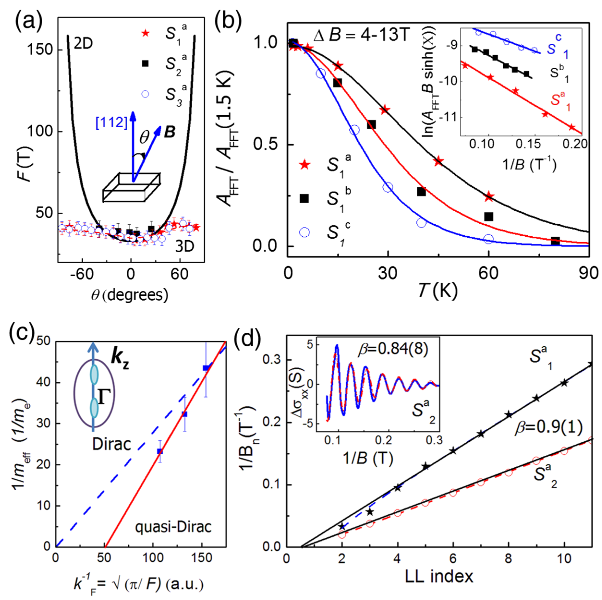

FIG. 2 (color online). Fermi surface parameters. (a) The angular dependence of SdH oscillation frequencies away from the (112) plane. The solid line is the expectation for a two-dimensional Fermi surface. (b) The temperature dependence of the oscillation amplitude that gives $m_{\rm eff}$ for different samples (S_1^a, S_2^a, and S_3^a). The inset shows the Dingle plots of the FFT amplitude for samples from different batches (a, b, and c). (c) Extracting the Fermi velocity from a linear fit of $1/m_{\rm eff}$ versus $\sqrt{(\pi/F)}$ (in atomic units, a.u.), as described in the main text (solid line). The dashed line indicates the expected behavior for a perfect Dirac system. The inset shows a schematic Fermi surface before and after the Lifshitz transition. (d) Index plot to extract the Berry phase for samples S_1^a and S_2^a (as detailed in the text). The inset shows quantum oscillations in conductivity σ_{xx} for S_2^a fitted to the Lifshitz-Kosevich formula (dashed line) [14] with a phase of $\beta = 0.84(8)$.

processes that deviate from the current path—i.e., the classical scattering time (transport time) is a measure of how long a particle moves along the applied electric field gradient. Thus, the quantum mobility is susceptible to small angle and large angle scattering, while the transport (classical) mobility is susceptible only to large angle scattering. The ratio μ_c/μ_q is a measure of the relative importance of small angle scattering; Table I suggests that small angle scattering dominates in all our samples, in particular, for lower doping n_{SdH}.

Linear magnetoresistance.—Now we discuss the origin of the unconventional linear MR in a transverse magnetic field for two crystals of Cd_3As_2 [shown initially in Fig. 1(a)] plotted in Fig. 3(a) on a log-log scale to emphasize the low-field behavior. We observe that the linear MR behavior is established above a crossover field B_L. Interestingly, we find that B_L and the relative change in magnetoresistance, $MR = \Delta\rho_{xx}(B)/\rho_{xx}(0)$, vary with temperature in the same ratio as the mobility μ_c and, consequently, the resistivity ratio ($\rho \sim \mu_c^{-1}$) [see Fig. 3(b)]. Furthermore, we find that all MR curves collapse onto a single curve in a Kohler plot for temperatures below 200 K, suggesting that a single relevant scattering process is dominant in Cd_3As_2, as shown in Fig. 3(c). Small deviations at higher temperatures are caused by the onset of phonon scattering, consistent with the Debye temperature of 200 K [22].

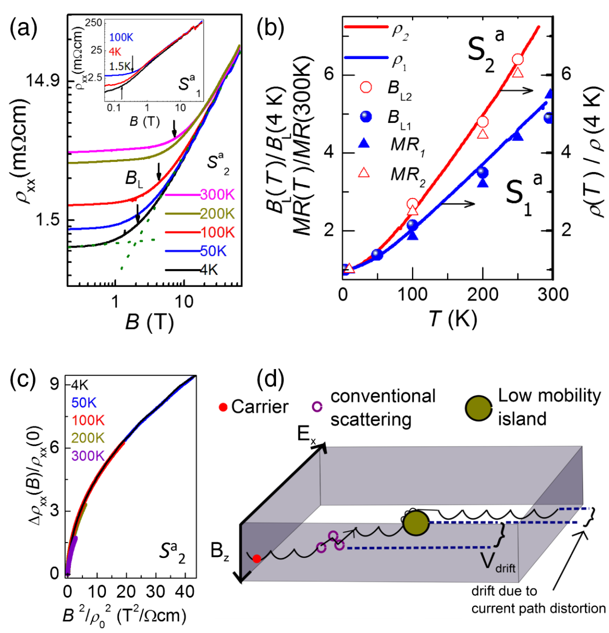

FIG. 3 (color online). Linear MR and mobilities. (a) Log-log plot of resistance versus field for S_2^a and S_1^a (inset). The crossover field B_L to the linear MR is indicated by arrows. (b) The temperature dependence of ratios of mobility, $\rho \sim \mu^{-1}{}_c$ (solid lines), B_L (squares) normalized to the 4 K values, and the change in MR (triangles) show the same temperature dependence. (c) Kohler's plots for S_2^a showing the collapse of all magnetoresistance curves into one curve (below the Debye temperature 200 K [22]). (d) Schematic diagram of scattering processes in Cd_3As_2.

The conventional MR shows a quadratic dependence at low fields and saturation for Fermi surfaces with closed orbits in high fields, such that $\mu_c B_L > 1$; in our samples the crossover field can be estimated as $B_L > 1$ T. Linear MR has been predicted by Abrikosov [25] to occur in the quantum limit, only beyond the $n = 1$ Landau level. However, in our crystals the value of B_L is much lower than the position of the $n = 1$ level above 32 T.

Another explanation for the presence of linear MR has its origin in classical disorder models. For example, linear MR was realized for highly disordered [26,27] or weakly disordered high-mobility samples [28], thin films, and quantum Hall systems [29]. The linear MR arises because the local current density acquires spatial fluctuations in both magnitude and direction, as a result of the heterogeneity or microstructure caused by nonhomogeneous carrier and mobility distribution [see Fig. 3(d)]. There are a series of experimental realizations of linear MR in disordered systems, such as $Ag_{2\pm\delta}Se$ and $Ag_{2\pm\delta}Te$ [30], two-dimensional systems (epitaxial graphite) [31,32], In (As/Sb) [33], $LaSb_2$ [34], and $LaAgSb_2$ [35,36].

Monte Carlo simulations for a system with a few islands of enhanced scattering embedded in a medium of high mobility [33] suggest that MR is linked to the generation of an effective drift velocity perpendicular to cycloid motion in an applied electric field caused by multiple small angle scattering of charge carriers by the islands [see Fig. 3(d)]. For such a mechanism the mobility μ_c is determined by the island separation, and, depending on the value of $(\delta\mu_c/\mu_c)$, the linear MR emerging from this process will be associated with $B_L \sim \mu_c^{-1}$, which tracks the island separation if $(\delta\mu_c/\mu_c) < 1$ and tracks $\delta\mu_c^{-1}$ if $(\delta\mu_c/\mu_c) > 1$. Thus, the absolute value of the linear MR and B_L would vary like μ_c^{-1} (linked to ρ values) [Fig. 3(b)]. This scaling is consistent with the classical disordered model originating from fluctuating mobilities for the observed linear MR in Cd_3As_2.

Last, we comment on the possible source of disorder in Cd_3As_2. STM measurements found disordered patches with a typical size of 10 nm and separated by distances of 50 nm, attributed to As vacancy clusters [5], likely to appear during the growth in a Cd-rich environment with a small width formation for Cd_3As_2 [9]. Assuming a disorder density comparable to the carrier concentration, n_{SdH}, and a dielectric constant of $\epsilon = 16$ (see Ref. [37]), one can estimate the classical mobility as being 30000 cm^2/V s for Cd_3As_2, which is similar to our measured classical mobilities μ_c. The lower quantum mobility μ_q corresponds to small angle scattering when carriers travel over the mean free path, $\ell \sim$ 110–150 nm, which is similar to the distribution of As vacancy clusters imaged by STM [5] [see Fig. 3(d)]. Furthermore, a mobility ratio $\mu_c/\mu_q > 1$ points towards As vacancies as being the small angle scatterers in

Cd_3As_2 [38]. Concerning the possible changes of the Fermi surface induced by a magnetic field in Cd_3As_2, our data that approach the quantum limit [for sample S_1^a in Fig. 1(c)], we find no evidence of additional frequencies (only spin splitting due to the large g factors) or changes in scattering (Dingle term) up to 65 T.

In conclusion, we have used ultrahigh magnetic fields to characterize the Fermi surface of Cd_3As_2 and to understand the origin of its linear magnetoresistance. The Fermi surface of Cd_3As_2 has an elliptical shape with a nontrivial Berry phase. We find that the linear MR enhancement scales with mobility in Cd_3As_2 and likely originates from fluctuating mobility regions that caused inhomogeneous current paths. Close to the quantum limit we find no evidence for Fermi surface reconstruction except the observed spin-splitting effects caused by the large g factors. The large and growth sample-dependent linear MR suggest a possible avenue for tuning sample quality and further enhancing its MR for useful practical devices.

We acknowledge and thank Igor Mazin for the band-structure calculations and comments on the manuscript. We acknowledge fruitful discussions with John Chalker, Steve Simon, Zohar Ringel, and Gabor Halasz and useful comments given by David Macdougal and S. L. Bud'ko. This work was mainly supported by EPSRC (EP/L001772/1, EP/I004475/1, EP/I017836/1). Part of the work was performed at the LNCMI, member of the European Magnetic Field Laboratory (EMFL). A. I. C. acknowledges an EPSRC Career Acceleration Fellowship (EP/I004475/1). Work done at Ames Lab was supported by the U.S. Department of Energy, Office of Basic Energy Science, Division of Materials Sciences and Engineering. Ames Laboratory is operated for the U.S. Department of Energy by Iowa State University under Contract No. DE-AC02-07CH11358. Y. C. acknowledges the support from the EPSRC (United Kingdom) Grant No. EP/K04074X/1 and a DARPA (United States) MESO project (No. N66001-11-1-4105).

*Corresponding author.
amalia.coldea@physics.ox.ac.uk

[1] Z. Wang, H. Weng, Q. Wu, X. Dai, and Z. Fang, Phys. Rev. B **88**, 125427 (2013).
[2] S. Borisenko, Q. Gibson, D. Evtushinsky, V. Zabolotnyy, B. Büchner, and R. J. Cava, Phys. Rev. Lett. **113**, 027603 (2014).
[3] N. Madhab *et al.*, Nat. Commun. **5**, 3786 (2014).
[4] Z. K. Liu *et al.*, Nat. Mater. **13**, 677 (2014).
[5] S. Jeon, B. B. Zhou, A. Gyenis, B. E. Feldman, I. Kimchi, A. C. Potter, Q. D. Gibson, R. J. Cava, A. Vishwanath, and A. Yazdani, Nat. Mater. **13**, 851 (2014).
[6] H. Yi *et al.*, Sci. Rep. **4**, 6106 (2014).
[7] J. Feng, Y. Pang, D. Wu, Z. Wang, H. Weng, J. Li, X. Dai, Z. Fang, Y. Shi, and L. Lu, arXiv:1405.6611.
[8] T. Liang, G. Quinn, N. Ali Mazhar, M. Liu, R. J. Cava, and N. P. Ong, Nat. Mater. **14**, 280 (2014).
[9] M. N. Ali, Q. Gibson, S. Jeon, B. B. Zhou, A. Yazdani, and R. J. Cava, Inorg. Chem. **53**, 4062 (2014).
[10] P. C. Canfield and Z. Fisk, Philos. Mag. B **65**, 1117 (1992).
[11] See Supplemental Material at http://link.aps.org/supplemental/10.1103/PhysRevLett.114.117201 for the band structure calculations and additional graphs for different samples supporting the findings of the main paper.
[12] P. Blaha, K. Schwarz, G. Madsen, D. Kvasnicka, and J. Luitz, WIEN2k, An Augmented Plane Wave + Local Orbitals Program for Calculating Crystal Properties, 2001.
[13] S. Bannerjee, Ph. D. dissertation, University of California, Davis, 2012.
[14] D. Shoenberg, *Magnetic Oscillations in Metals* (Cambridge University Press, Cambridge, England, 1984).
[15] S. G. Sharapov, V. P. Gusynin, and H. Beck, Phys. Rev. B **69**, 075104 (2004).
[16] I. A. Luk'yanchuk and Y. Kopelevich, Phys. Rev. Lett. **93**, 166402 (2004).
[17] M. Singh and P. Wallace, Solid State Commun. **45**, 9 (1983).
[18] P. R. Wallace, Phys. Status Solidi (b) **92**, 49 (1979).
[19] A. A. Taskin and Y. Ando, Phys. Rev. B **84**, 035301 (2011).
[20] L. He, X. Hong, J. Dong, J. Pan, Z. Zhang, J. Zhang, and S. Li, Phys. Rev. Lett. **113**, 246402 (2014).
[21] A. R. Wright and R. H. McKenzie, Phys. Rev. B **87**, 085411 (2013).
[22] K. Bartkowski, G. Pompe, and E. Hegenbarth, Phys. Status Solidi (a) **111**, K165 (1989).
[23] I. Rosenman, J. Phys. Chem. Solids **30**, 1385 (1969).
[24] F. Blom, J. Cremers, J. Neve, and M. Gelten, Solid State Commun. **33**, 69 (1980).
[25] A. A. Abrikosov, Phys. Rev. B **58**, 2788 (1998).
[26] M. M. Parish and P. B. Littlewood, Nature (London) **426**, 162 (2003).
[27] J. Hu, M. M. Parish, and T. F. Rosenbaum, Phys. Rev. B **75**, 214203 (2007).
[28] C. Herring, J. Appl. Phys. **31**, 1939 (1960).
[29] S. H. Simon and B. I. Halperin, Phys. Rev. Lett. **73**, 3278 (1994).
[30] J. Hu and T. F. Rosenbaum, Nat. Mater. **7**, 697 (2008).
[31] M. A. Aamir, S. Goswami, M. Baenninger, V. Tripathi, M. Pepper, I. Farrer, D. A. Ritchie, and A. Ghosh, Phys. Rev. B **86**, 081203 (2012).
[32] A. L. Friedman *et al.*, Nano Lett. **10**, 3962 (2010).
[33] N. V. Kozlova, N. Mori, O. Makarovsky, L. Eaves, Q. D. Zhuang, A. Krier, and A. Patanè, Nat. Commun. **3**, 1097 (2012).
[34] S. L. Bud'ko, P. C. Canfield, C. H. Mielke, and A. H. Lacerda, Phys. Rev. B **57**, 13624 (1998).
[35] K. Myers, S. Bud'ko, I. Fisher, Z. Islam, H. Kleinke, A. Lacerda, and P. Canfield, J. Magn. Magn. Mater. **205**, 27 (1999).
[36] K. Wang and C. Petrovic, Phys. Rev. B **86**, 155213 (2012).
[37] B. Skinner, Phys. Rev. B **90**, 060202 (2014).
[38] S. Das Sarma and F. Stern, Phys. Rev. B **32**, 8442 (1985).